



Crustal and upper mantle seismic structure of the Svalbard Archipelago from the receiver function analysis

Monika WILDE-PIÓRKO

*Instytut Geofizyki, Wydział Fizyki, Uniwersytet Warszawski,
ul. Pasteura 7, 02-093 Warszawa, Poland <e-mail: mwilde@igf.fuw.edu.pl>*

Abstract: Receiver function provides the signature of sharp seismic discontinuities and the information about the shear wave (S-wave) velocity distribution beneath the seismic station. This information is very valuable in areas where any or few reflection and/or refraction studies are available and global and/or regional models give only rough information about the seismic velocities. The data recorded by broadband seismic stations have been analysed to investigate the crustal and upper mantle structure of the Svalbard Archipelago. Svalbard Archipelago is a group of islands located in Arctic, at the north-western part of the Barents Sea continental platform, which is bordered to the west and to the north by passive continental margins. The new procedure of parameterization and selection of receiver functions (RFs) has been proposed. The back-azimuthal sections of RF show a strong variation for the HSPB and KBS stations. Significant amplitudes of transversal component of RF (T-RF) for the HSPB station indicate a shallow dipping layer towards the southwest. The structure of the crust beneath the SPITS array seems to be less heterogeneous, with very low amplitudes of converted phase comparing to the KBS and HSPB stations. Forward modelling by trial-and-error method shows a division of the crust into 3–4 layers beneath all stations and layering of the uppermost mantle beneath the SPITS array and the HSPB stations. The thickness of the mantle transition zone is larger for western part of archipelago and smaller for eastern part comparing to *iasp91* model.

Key words: Arctic, Svalbard, teleseismic waves, seismogram rotation, parameterization, quality check.

Introduction

Receiver function technique is already well established method to investigate the crustal and upper mantle structure, locally providing the signature of sharp seismic discontinuities and the information about the shear wave (S-wave) velocity distribution beneath the seismic station. This information is very valuable in areas where any or few reflection and/or refraction studies are available and global and/or regional models give only rough information about the seismic velocities.

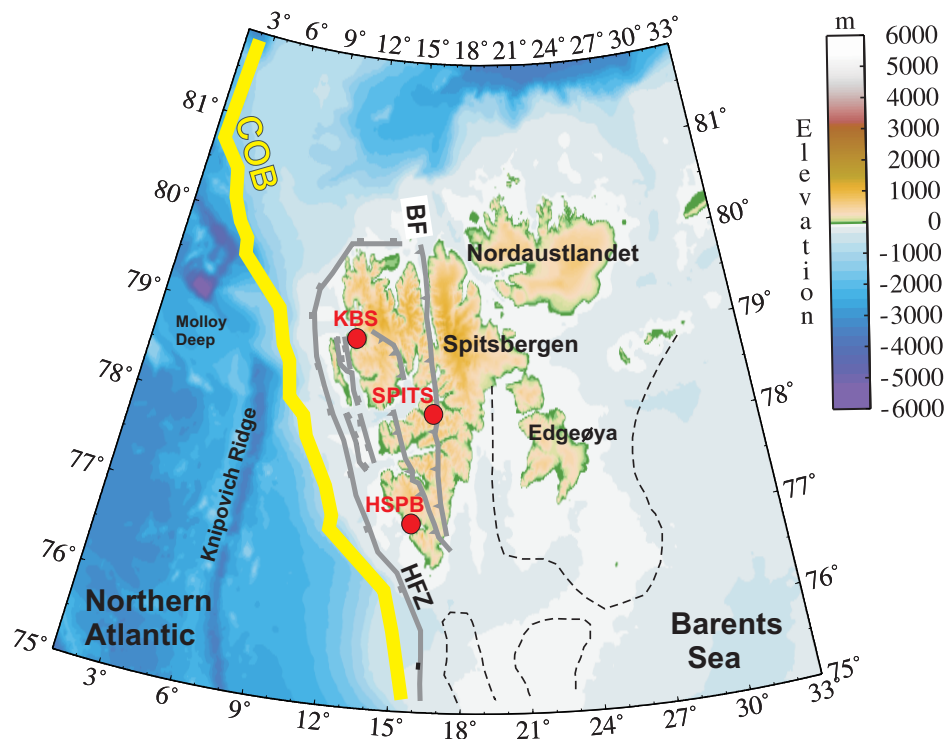


Fig. 1. Location of the KBS and HSPB broad-band seismic stations and the SPITS array (red circle) on the background of the topography/bathymetry map and simplified tectonic elements of the Svalbard Archipelago. COB – continent-ocean boundary; main fault zones: BF – Billefjorden Fault; HFZ – Hornsund Fault Zone. See text and Table 1 for details.

Polar regions are usually such areas, so the data recorded by eight broadband seismic stations: HSPB (Hornsund), KBS (Kingsbay) and SPITS array (Spitsbergen Array) have been analysed by receiver function methods to locally investigate the crustal and upper mantle structure of the Svalbard Archipelago in Arctic.

The Barents Sea continental shelf has been affected by several phases of tectonism since the Precambrian times (*e.g.* Talwani and Eldholm 1977; Birkenmajer 1981; Hjeller 1993). The oldest formations, including Precambrian, Cambrian and Ordovician rocks occur as a belt along the west and north coast of Spitsbergen and generally had been very strongly metamorphosed during repeating orogenies *ca.* 1700, 1000 and 600 MY ago. During the Caledonian Orogeny in Silurian, large-scale folding and faulting happened due to the collision of Baltica and Laurentia, affecting mainly the eastern part of Svalbard (Sellevoll *et al.* 1991). In Devonian time, the present-day eastern Spitsbergen and Nordaustlandet moved northward along the Billefjorden Fault (Fig. 1) and the eastern part of the Svalbard Archipelago attached to the western Spitsbergen (Sellevoll *et al.* 1991; Harland 1997). During the Jurassic and lowermost Cretaceous, most of the Svalbard was covered by a shallow sea, to be later uplifted and eroded. In the Early Eocene, the

continental break-up occurred and sea floor spreading started along the Reykjanes, Aegir and Mohns Ridges (Talwani and Eldholm 1977). The shearing along the faults between northeast Greenland and Svalbard has resulted in the Western Spitsbergen Orogeny, causing intense folding of the Spitsbergen west-coast strata, as well as the formation of a depression basin to the east (Steel *et al.* 1985). In Early Oligocene, a change of the spreading direction from NNW-SSE to NW-SE has resulted in the termination of the Western Spitsbergen Orogeny (Talwani and Eldholm 1977).

During the last ten years, a significant progress in integrating data for Barents Sea and surrounding areas has been made (Levshin *et al.* 2007; Ritzmann *et al.* 2007; Ritzmann and Faleide 2009; Hauser *et al.* 2011; Klitzke *et al.* 2015). Typical resolution of regional seismic model is 50 km in horizontal direction and 5 km in vertical direction. Receiver function methods are relatively cheap and easy tools, comparing with reflection and refraction profiling, to locally collect information about the seismic structure of the crust and upper mantle and to complement the regional models.

Data and methodology

Receiver function analysis has been used to investigate the crustal and upper mantle structure in the Spitsbergen area beneath the broadband seismic stations: HSPB (Hornsund), KBS (Kingsbay) and the SPITS array (Spitsbergen array stations: SPA, SPB1–5). The facilities of the IRIS Data Management System, and specifically the IRIS Data Management Centre, were used for access to waveform and metadata required in this study. Stations of SPITS array are handled as 5 stations located in one place (central point of array), because the aperture of the array, 1 km, is much smaller than the Fresnel zone of teleseismic waves. Locations of the seismic stations are shown in Fig. 1. Coordinates of seismic stations, a type of broadband sensor, time range of data set, total number of events in a distance range of 30–100° with magnitude ≥ 5.5 and the number of events selected for final interpretations are shown in Table 1. Distributions of epicentres of teleseismic events selected for final interpretations are also plotted relatively to a position of station in Fig. 2. The back-azimuthal coverage of epicentres is very good, however, most of the events are concentrated in the back-azimuth range of 0–180°.

Receiver function technique is now well known method of investigation of a structure located beneath a seismic station based on three-component seismograms of teleseismic events (*e.g.* Langston 1977; Vinnik 1977). Thanks to the deconvolution procedure, source time function, ray-path influence and instrument transfer function should be removed from horizontal components of seismograms, resulting in function which contains only an impulse response of the structure beneath a seismic station. To calculate the receiver function (RF) few steps are usu-

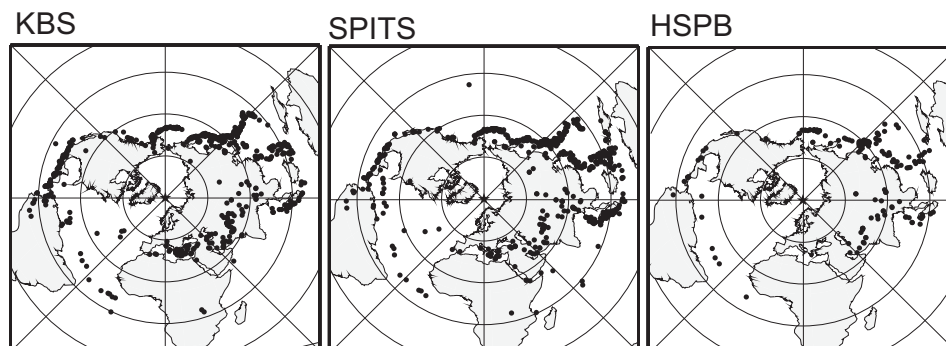


Fig. 2. Distribution of epicentres of teleseismic events with magnitude 5.5 (from USGS/NEIC Catalogue) selected for final interpretations. The equidistant projection shows the true distances and back-azimuths of the epicentres with respect to each seismic station. See Table 1 for details.

ally done (e.g. Owens *et al.* 1984; Kind *et al.* 1995; Geissler *et al.* 2005): (1) preparing a list of teleseismic events occurred during the analysed time with the desired magnitude and epicentral distance; (2) selection of three-component seismograms with high signal-to-noise ratio; (3) restitution filtering of seismograms and/or low-pass or band-pass filtering of seismograms; (4) picking the onset of direct wave or calculating the onset based on one-dimensional global model; (5) cutting the seismograms in time window, usually tens of seconds before and tens of seconds after the onset of direct wave; (6) rotation from Z, N, E components into Z, R, T components or into a ray coordinate system (L, Q, T) based on theoretical back-azimuth and incident angles of rays or angles calculated from polarization analysis of seismograms; (7) deconvolution of a vertical component from horizontal components in frequency domain or in time domain; (8) normalization of components of receiver function to preserve the absolute amplitude; (9) manual quality check of the calculated receiver function. Later, receiver functions can be move-out corrected and stacked in distance or back-azimuth bins to improve sig-

Table 1
Location of seismic broadband stations from International Seismological Centre and time range of used data set for receiver function analysis.

Station's code	Latitude [°]	Longitude [°]	Elevation [m]	Broadband sensor	Time range of data set	Total number of events	Number of selected RF
HSPB	77.0019 N	15.5332 E	10.0	STS-2	09.2007–03.2012	1095	335
KBS	78.9256 N	11.9417 E	74.0	STS-1VBB	11.1994–12.2009	2258	823
SPA0	78.1777 N	16.3700 E	323.0	CMG-3TB	09.2004–03.2012	1156	570
SPB1	78.1796 N	16.3906 E	301.0	CMG-3TB	09.2004–03.2012	1188	670
SPB2	78.1742 N	16.3846 E	200.0	CMG-3TB	09.2004–03.2012	1181	734
SPB3	78.1737 N	16.3584 E	234.0	CMG-3TB	09.2004–03.2012	1191	709
SPB4	78.1789 N	16.3482 E	340.0	CMG-3TB	09.2004–03.2012	1135	609
SPB5	78.1823 N	16.3683 E	295.0	CMG-3TB	09.2004–10.2011	1076	625

nal-to-noise ratio. The above procedures are time-consuming for big data sets and depend on the experience of the researcher, particularly during the selection of seismograms, a length of the time window, deconvolution parameters and finally in quality check of calculated receiver functions. In order to resolve these issues, a new automatic procedure of calculation, quality check and selection of receiver function has been proposed. The main difference is that receiver functions are calculated for all seismograms of teleseismic events, which occurred during the analysed time range with magnitude above some threshold. A new procedure of rotation of seismograms from Z, N, E to L, Q, T components are used. Each receiver function is parameterized by several quantities. These quantities are later used for quality check and selection of receiver functions.

In details, a new procedure used in this work to calculate a receiver function for teleseismic P-waves is as follows: (1) preparing the list of events occurred during the analysed time with magnitude equal or greater than 5.5 and an epicentral distance range of 30–100°; (2) cutting seismograms based on the prepared event list 300s before and 300s after the theoretical P-onset calculated for the *iasp91* model (Kennett and Engdahl 1991); (3) scaling the components of seismograms due to different sensitivity of components; (4) one-pass low-pass filtering with Butterworth filter with corner frequency 5 Hz; (5) resampling seismograms to 20 Hz; (6) cutting the seismograms in time window 100 s before and 100 s after the onset of direct P wave calculated due to *iasp91* model; (7) calculation of Q-RF and T-RF in to steps: (a) calculation of R-RF by time-domain Wiener deconvolution of R component of seismogram with Z component for back-azimuths from 0° to 180° every 5° and searching R-RF for which energy at time 0 s is maximal (it is equivalent of rotation of seismograms from Z, N, E components to Z, R, T); (b) calculation of Q-RF by time-domain Wiener deconvolution of Q component of seismogram with L component for back-azimuth found in (a) and for polarization angles from 0° to 50° every 1° and searching Q-RF for which the energy at time 0 s has minimum (it is equivalent to rotation of seismograms from Z, R, T component to L, Q, T); (8) the final traces L-RF, Q-RF and T-RF are results of convolution of the L, Q, T components of seismogram, rotated from Z, N, E components for back-azimuth and polarization angle found in (7), with the inverse-filter generated from L component for each earthquake and normalized to amplitude of direct P wave; (9) calculation of parameters (quantities) of L-RF, Q-RF and T-RF and quality check of the Q-RF and T-RF based on these parameters (Table 2). The software package Seismic Handler (Stammler 1993) and the public domain GMT software (Wessel and Smith 1998) were used for most of data processing and plotting.

The Q-RF for one-dimensional structure contains only the P-to-S converted phases with P multiples removed (Ammon 1991). Delay time of converted phase depends on the depth of the discontinuity and the S-wave velocity above the discontinuity. Amplitude of the converted phase depends on the contrast of seismic velocities at the boundary. The seismic energy is not observed on the T-RF. These

Table 2
List of parameters and their values used for selection of Q-RF and T-RF.

Name of parameter	Parameter's type	Minimal value	Maximal value	Time range used for calculation of parameter	Component
ex0a	maximal amplitude	0.0	0.3	from -80 s to -1 s	absolute value of LRF
ex0b	maximal amplitude	0.0	0.3	from 1 s to 80 s	absolute value of LRF
ex1	rms	0.0	0.04	from -70 s to -30 s	QRF, TRF
ex2	rms	0.0	0.04	from -30 s to -10 s	QRF, TRF
ex3	rms	0.0	0.04	from -10 s to 0.0	QRF, TRF
ex4	rms	0.04	0.1	from 0 s to 10 s	QRF, TRF
ex5	rms	0.02	0.08	from 10 s to 30 s	QRF, TRF
ex6	rms	0.01	0.05	from 30 s to 70 s	QRF, TRF
ex8	rms	0.02	0.07	from -70 s to 70 s	QRF, TRF
ex9	maximal amplitude	0.0	5.0	from 0.0 Hz to 0.03 Hz	absolute value of spectrum of Q-RF or T-RF

conclusions are also valid for more complicated laterally homogeneous media with dipping discontinuities or seismic anisotropy. But then, the energy of converted waves contributes also to the T-RF with different pattern in both cases (Cassidy 1992).

Modelling and results

Receiver functions must be stacked in distance or back-azimuth bins to improve signal-to-noise ratio. The simplest approach is to stack all Q-RF and T-RF, respectively for each station. In Fig. 3, there are shown stacked Q-RF and T-RF for the seismic stations: KBS, HSPB and for the SPITS array calculated and selected with procedure proposed above. Each RF was move-out corrected for slowness 6.4 s° . The strongest amplitudes of Q-RF and T-RF are observed for the HSPB station, the weakest for the SPITS array. For each station 3–4 dominant converted phases (positive or negative) are observed in time intervals 0–5 s (marked by arrows in Fig. 3). The rough delay time of any multiple can be calculated from a rule-of-thumb: for a PpPms multiple it is three times delay time of P-to-S converted phase at considered discontinuity and for PsPms and PpPms multiples – four times delay time of P-to-S converted phase at considered discontinuity. In this way, starting from earliest observed phases of Q-RF it is quite easy to estimate which phases are converted at discontinuity and which are just multiples. A more detailed study of Q-RF and T-RF for each station can be done thanks to back-azimuth sections of RF in 54 bins of 6.6° wide (Fig. 4). The overlapping bins in each case were 50%. The most scattered and/or noisy RFs are observed in back-azimuth intervals $200\text{--}240^\circ$ and $300\text{--}340^\circ$ because of a low number of RF in that ranges (see Fig. 2). For each station we can observe a strong conversion from the uppermost crust (d1 – dark grey lines in Fig. 4) and its negative multiple (next to d1 –

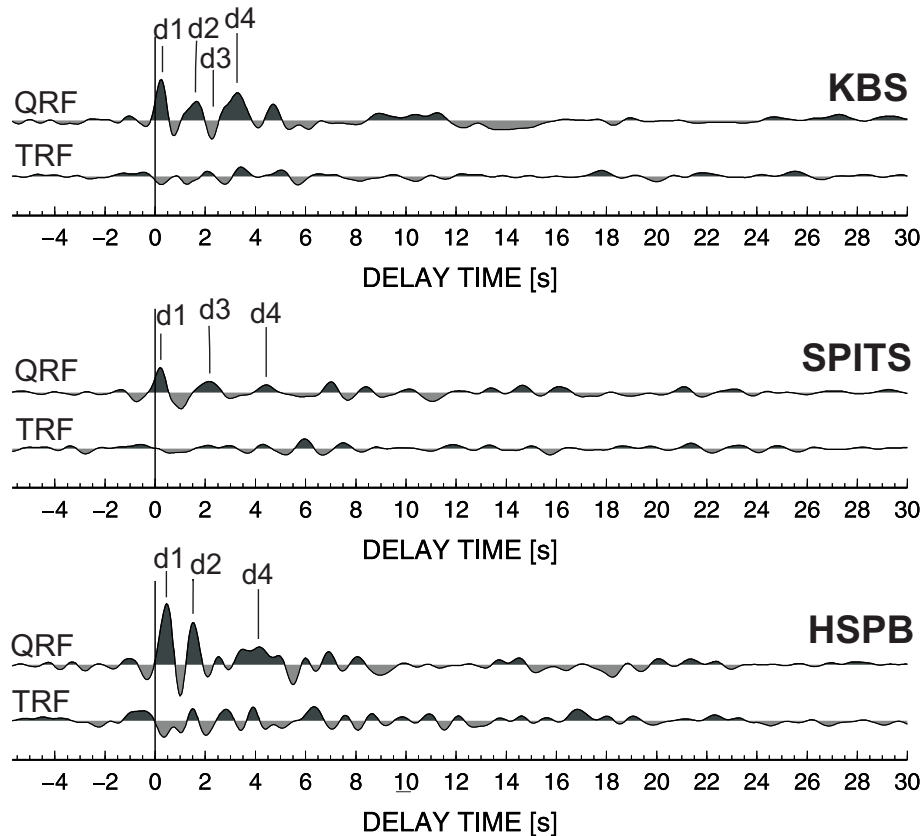


Fig. 3. Stacked Q-RF and T-RF for the KBS and HSPB stations and the SPITS array. The amplitude scale is the same for all components. Time zero refers to the direct P wave. The P-to-S conversion phases from the discontinuity in the uppermost crust (d1), in the upper crust (d2) and in the lower crust (d3) and from the Moho discontinuity (d4) are marked by arrows. RFs are filtered with band-pass Butterworth filter of corner frequencies 0.01 and 1 Hz.

light grey lines in Fig. 4). In the crust, there are well visible two discontinuities beneath the KBS station (d2 and d3 – dark grey lines in Fig. 4) and one discontinuity beneath the SPITS array (d3 – dark grey line in Fig. 4) and HSPB station (d2 – dark grey line in Fig. 4). The phases converted at the Moho discontinuity arrived about 3.5–4.5 s after the direct P wave (d4 – dark grey lines in Fig. 4). T-RFs of the HSPB station show strong, back-azimuthal dependence of amplitudes of phase d1 and d2 with periodicity of 180°, amplitudes changed the sign from positive to negative around 50° and from negative to positive around 230°. Due to the theoretical modelling of RF in homogeneous media with dipping discontinuities (*e.g.* Cassidy 1992), that points out to the existence of layer dipping in the southwest direction in the middle crust beneath that station. Amplitudes of T-RF of the KBS station show a different pattern, converted phases are strong only for some back-azimuth (*e.g.* of 70–180°, ellipse in Fig. 4) or changed sign with periodicity of 90°, what is the

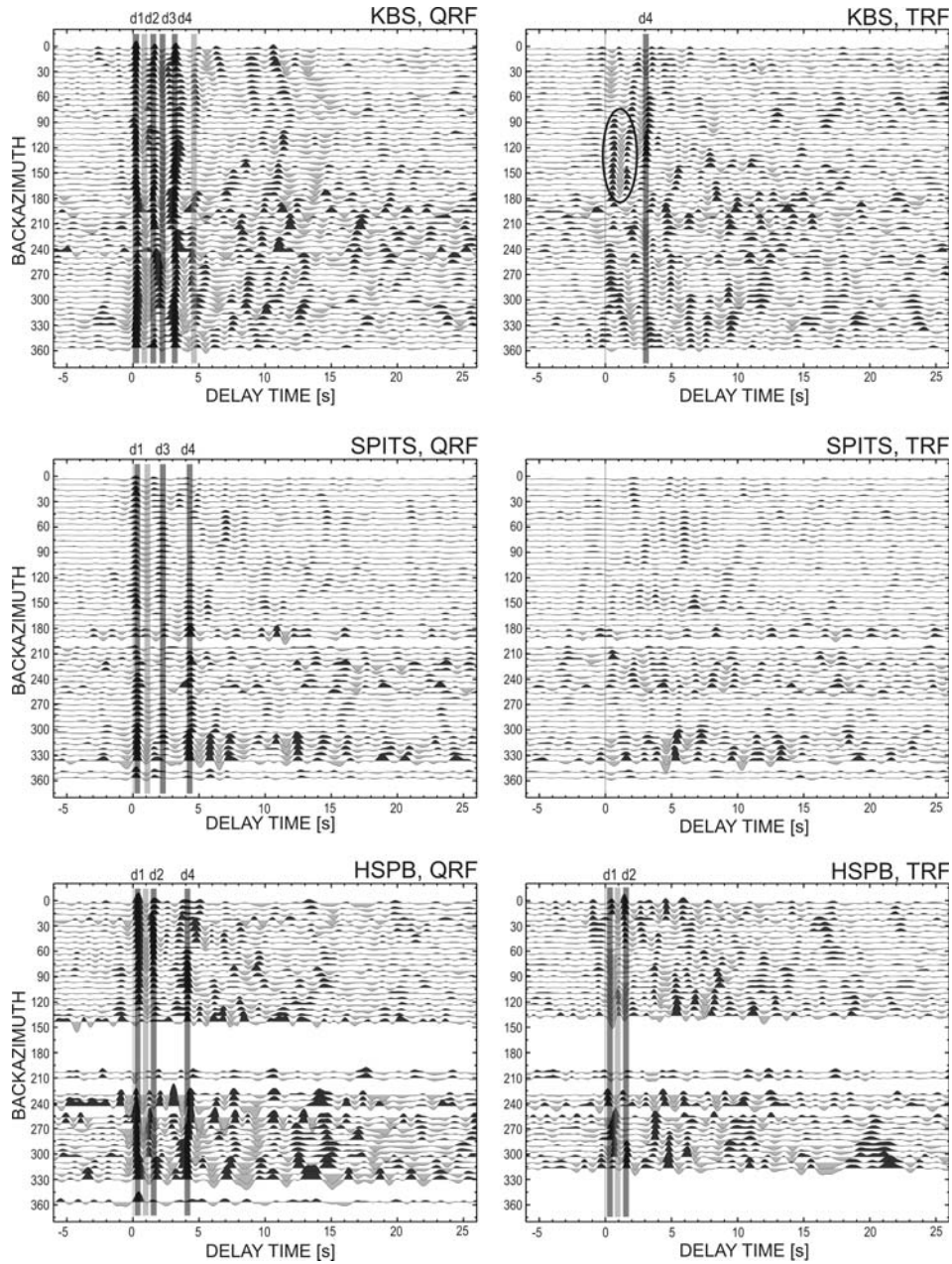


Fig. 4. Stacked receiver functions (Q-RF and T-QRF components) for the KBS and HSPB stations and the SPITS array, sorted versus back-azimuth. The amplitude scale is the same for all components. Time zero refers to the direct P waves. The P-to-S conversion phases from the uppermost discontinuity (d1), the upper crust (d2) and lower crust (d3) and Moho discontinuity (d4) are marked by thick dark lines and associated multiples by thick light lines. Ellipse marks the strong converted phases of T-RF of the KBS station. RFs are filtered with band-pass Butterworth filter of corner frequencies 0.01 and 1 Hz.

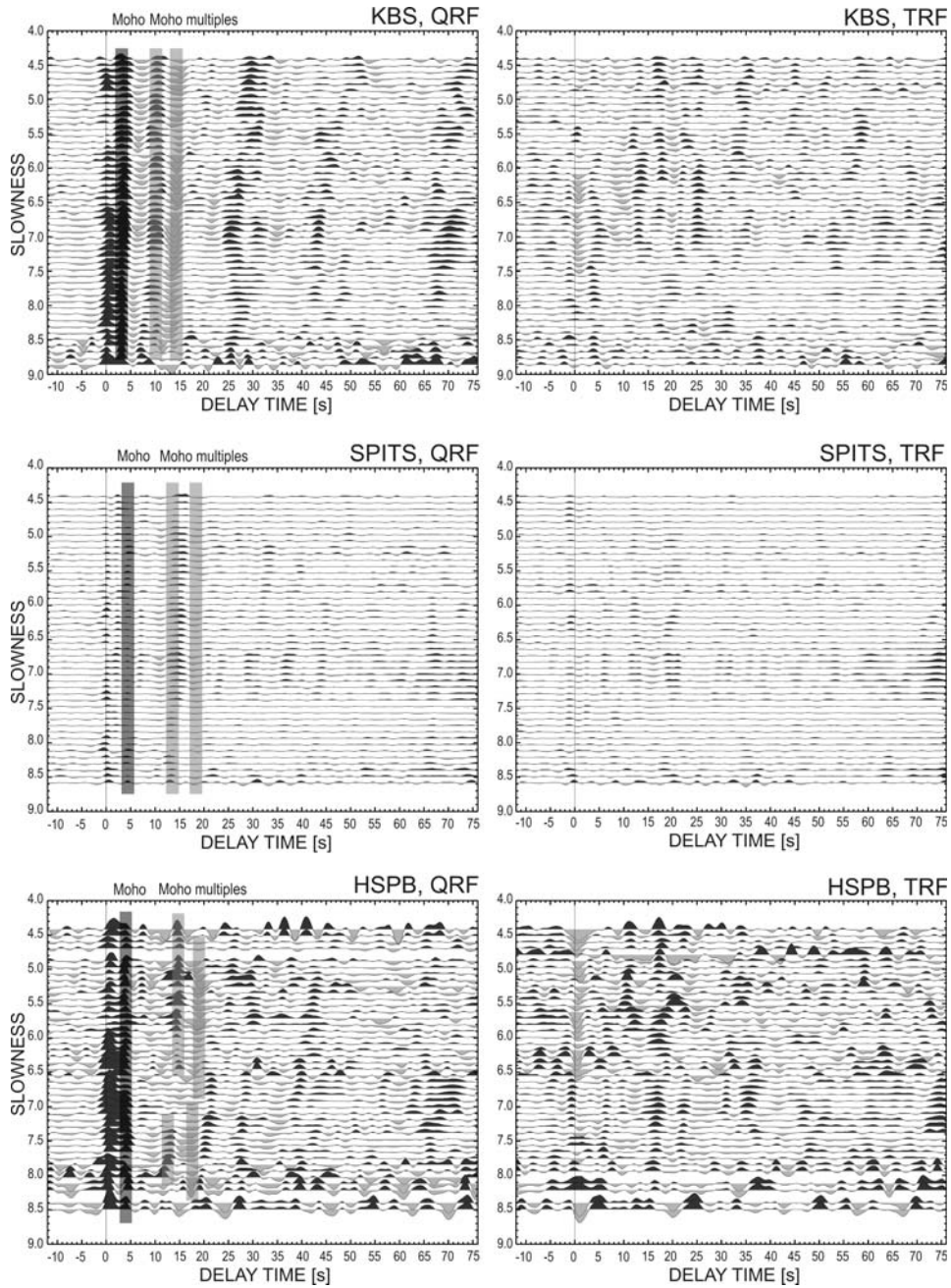


Fig. 5. Stacked receiver functions (Q-RF and T-QRF components) for the KBS and HSPB stations and the SPITS array, sorted versus slowness. The amplitude scale is the same for all components. Time zero refers to the direct P waves. The P-to-S conversion phases from the Moho discontinuity are marked by thick dark lines and associated multiples by thick light lines. RFs are filtered with band-pass Butterworth filter of corner frequencies 0.01 and 0.25 Hz.

influence of seismic anisotropy existing beneath the station (*e.g.* Cassidy 1992). But at the same time, these phases experience significant differentiation of time delay depending on the back-azimuth, which is a typical feature for a dipping discontinuity. That could suggest that both strong seismic anisotropy and dipping discontinuity exist beneath the KBS stations in the middle crust. However, d4 phase changes its amplitude with periodicity of 180° , amplitude change the sign from negative to positive around 30° , and from positive to negative around 210° , what means that the Moho discontinuity dips towards south-west direction.

We can estimate also an average crustal Poisson's ratio σ and crustal thickness Z_m following the approach of Zhu and Kanamori (2000). In a grid search over the σ - Z_m space, we can determine the (σ, Z_m) pair which is in closest agreement with the observed P-to-S converted wave (Ps) from the Moho discontinuity and its multiples, PpPms and PsPms+PpPms waveforms. The AH++ packages written by Dr. Joachim Saul have been used for simultaneous calculation of a crustal thickness and a Poisson's ratio. Figure 5 shows slowness sections of Q-RF and T-RF for the seismic stations: KBS, HSPB and for the SPITS array; Ps from the Moho discontinuities is marked by dark grey line and its multiples by light grey lines. Each RF was move-out corrected for slowness 6.4 s° and stacked in 54 slowness bins of 0.09 s° wide. The overlapping bins in each case were 50%. The values of mean Vp in the crust, necessary for Poisson's ratio and crustal thickness estimation were calculated from the BARENTS50 model (Ritzmann *et al.* 2007) and there were 6.3 , 5.9 and 6.0 km s^{-1} , respectively beneath the KBS and HSPB stations and the SPITS array. For the stack of all events with equal weight of Ps and its multiples, the average crustal Poisson's ratio is 0.28 ± 0.07 and crustal thickness is $25 \pm 3 \text{ km}$ for the KBS station, 0.24 ± 0.08 and $33 \pm 3 \text{ km}$ for the SPITS array and 0.21 ± 0.08 and $32 \pm 3 \text{ km}$ for the HSPB station (Fig. 6).

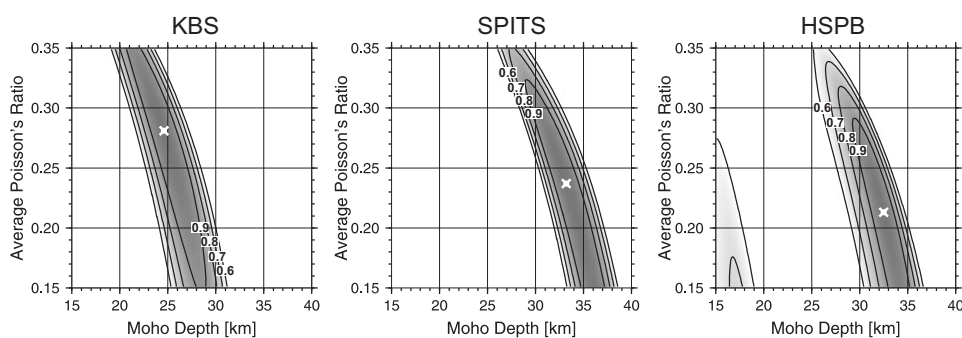


Fig. 6. Results of simultaneous crustal thickness and Poisson's ratio determination using the method of Zhu and Kanamori (2000) for the KBS and HSPB stations and the SPITS array. RFs are filtered with band-pass Butterworth filter of corner frequencies 0.06 and 0.167 Hz. The optimum value was found by grid searching within a depth interval of 15–40 km and 0.15–0.35 for Poisson's ratio. Amplitudes are normalized in the range from 0 to 1. White area corresponds to low amplitudes (0–0.6), grey corresponds to a fit better than 0.6, and the white cross in the darkest area shows the best fit.

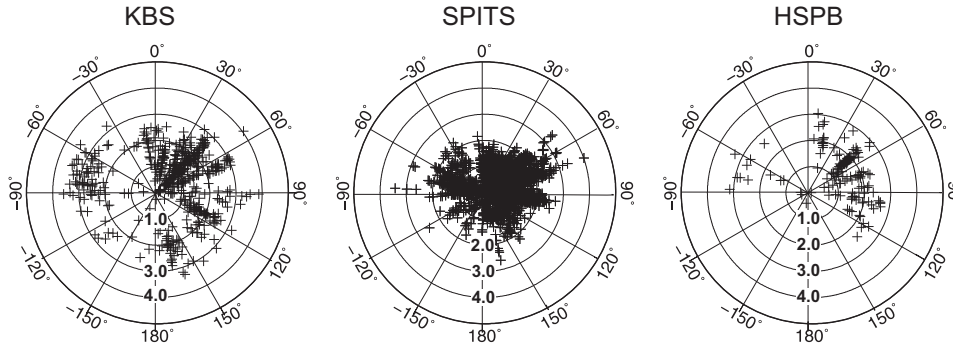


Fig. 7. Back-azimuthal distribution of near-surface S-wave velocity measurements beneath the KBS and HSPB stations and the SPITS array.

Receiver function technique can also help in estimation of near-surface S-wave velocity (V_s) beneath the seismic station (Saul *et al.* 2000), based on measurement of amplitude of R-RF at time 0 second. Results of this investigation show very low V_s : 1.7 ± 0.8 , 1.7 ± 0.6 and 1.0 ± 0.5 km s^{-1} , respectively beneath the KBS and HSPB stations and the SPITS array (Fig. 7). These values were the starting point for forward modelling of V_s beneath each station. By trial-and-error method, one-dimensional distribution of V_s with depth was found for each station to best fit

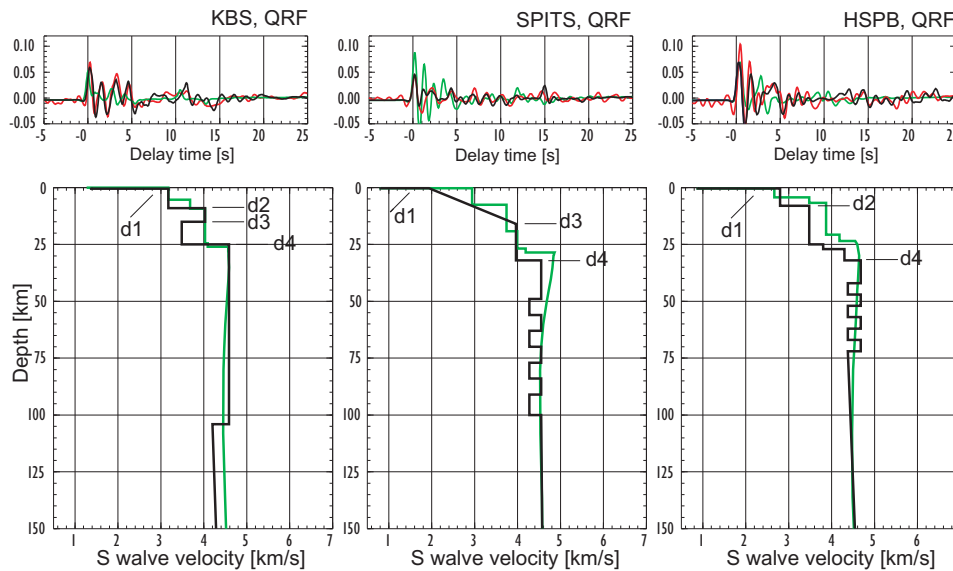


Fig. 8. Models of the crust and uppermost mantle – results of forward modeling (black line) of stacked Q-RF for the KBS and HSPB stations and the SPITS array; green line at S-wave velocity distribution shows the BARENTS50 model (Ritzmann *et al.* 2007). Above each S-wave velocity distribution, the fit between the observed receiver function (red line) and the synthetic ones calculated for final model (black line) and BARENTS50 model (green line) were shown. See Fig. 4 for more explanation.

the observed stacked Q-RF (Fig. 8). The synthetic Q-RFs were calculated using reflectivity method (Müller 1985) in InvRF packages written by Dr. Joachim Saul. The V_p/V_s has been assumed as ~ 2.0 , 1.73 and 1.8 for velocities in the sediments, consolidated crust and the mantle, respectively. The density was calculated from V_p from combined formulas of Gardner *et al.* (1974) and Berteussen (1977). The characteristic feature of the structure beneath each station was a very thin layer of 500, 300 and 200 meters width and very low V_s equal to 1.4, 0.9 and 0.8 km s⁻¹ associated with poorly consolidated ground, respectively for the KBS and HSPB stations and the SPITS array. Beneath the KBS station there was observed a high S-wave velocity zone ($V_s = 4.0$ km s⁻¹) in the middle crust and lower crust has a quite low S-wave velocity ($V_s = 3.5$ km s⁻¹), similar to that beneath the HSPB station. The gradient of V_s is observed beneath the SPITS array in the upper and middle crust, without marked boundary between these two units. For the SPITS array and HSPB station the layering of the uppermost mantle is observed too, down to a depth of 100 and 75 km, respectively for each station, due to prominent converted phases of positive and negative amplitudes (± 0.02) in 7–10 and 6–8 seconds time intervals. Summary of results obtained from forward modelling of receiver function and grid search over σ - Z_m space are shown in Table 3.

Table 3
S-wave distribution with depth beneath the KBS and HSPB stations and the SPITS array obtained from receiver function analysis in this study.

Station's code	Uppermost crust		Upper crust		Middle crust		Lower crust		Moho	Poisson's ratio of the crust	Uppermost mantle
	Depth interval [km]	V_s [km/s]	Depth interval [km]	V_s [km/s]	Depth interval [km]	V_s [km/s]	Depth interval [km]	V_s [km/s]	Depth [km]		V_s [km/s]
KBS	0–0.5	1.38	0.5–9.0	3.18	9.0–15.0	4.03	15.0–25.0	3.48	25±3	0.28±0.07	4.58
SPITS	0–0.2	0.81	0.2–16 km: 1.94–3.96 km/s		16.0–32.0		16.0–32.0	3.96	33±3	0.24±0.08	4.55
HSPB	0–0.3	0.88	0.3–8.0	2.80	8.0–25.0	3.48	25.0–32.0	3.80–4.30	32±3	0.21±0.08	4.68

To map the upper mantle seismic discontinuity, stacking of Q-RFs according to a piercing point of converted phase at the examined discontinuity is necessary because of sampling of a large area by waves converted at greater depths (diamonds and crosses in Fig. 9). Delay times of P-to-S converted phases from discontinuity at the 410 km depth plotted along longitudinal profiles show almost no deviation from the *iasp91* model (Fig. 9a), while phases from the depth of 660 km come 1.6–2.5 seconds later for western part of archipelago and 0.7–1.5 seconds earlier for eastern part (Fig. 9b). Q-RFs stacked along latitudinal profiles show deviation from the *iasp91* model only for southern Svalbard – converted phases from the depth of 410 and 660 km come 2 seconds earlier than it is predicted by *iasp91* model (Fig. 9a, b). The same pattern is observed if Q-RFs are stacked in 25 bins of a longitude width of 9° and a latitude width of 2° (Fig. 9c, d). The overlapping bins in each case were 50%. The converted phases from the

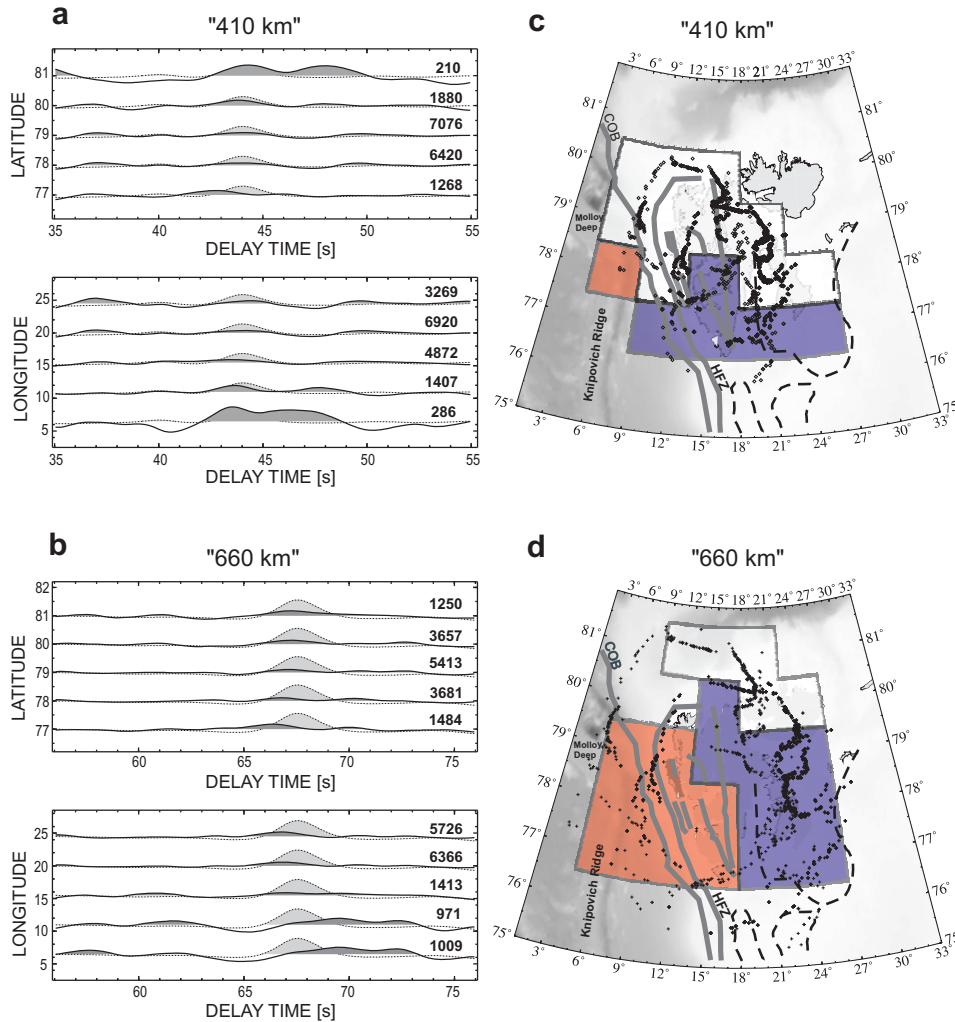


Fig. 9. Q-RFs (dark colour) plotted along latitudinal and longitudinal profiles due to piercing-points of P-to-S converted waves from “410 km” (a) and “660 km” (b) discontinuities, respectively. Q-RFs marked by light colour are calculated from the *iasp91* model (Kennett and Engdahl 1991). Differences of delay time between the *iasp91* model and observed P-to-S converted waves from “410 km” (c) and “660 km” (d) are marked by red (positive), blue (negative) and white (no difference) colour. Diamonds (c) and crosses (d) mark the piercing-points of P-to-S converted waves from “410 km” and “660 km” discontinuities, respectively.

depth of 410 km show no deviation from *iasp91* model for northern and central part of Svalbard, while for the southern part these phases come earlier comparing to *iasp91* model. The conversion phases from the depth of 660 km show no deviation from *iasp91* model for northern part of Svalbard, while for central and south areas the differentiation is visible between the western (later) and eastern part (earlier).

Discussion

The KBS and HSPB stations are located in the West Spitsbergen Fold-and-Thrust Belt (Hjeller 1983), east of the Hornsund Fault Zone marking the Continental-Ocean Boundary (COB) to the west. That location is very well seen in a complex pattern of the back-azimuthal sections of T-RF. The shallowest layer observed in RF models (above d1 – black line in Fig. 8) is most probably related to the sediments deposited as glacial debris flows (*e.g.* Solheim *et al.* 1998) and is also postulated in BARENTS50 model (green line in Fig. 8). The d2 discontinuity beneath the KBS and HSPB stations (Figs 4 and 8) marks the top of crystalline crust, however in regional models (Ritzmann *et al.* 2007; Klitzke *et al.* 2015) it is observed at the depth of 5 and 4 km, not 9 and 8 km, respectively. Also from refraction profiles (Czuba *et al.* 2008; Czuba 2013; Krysiński *et al.* 2013) going closely to the KBS and HSPB stations, the depths to the top of crystalline crust are 5 and 4 km, respectively. Additionally, on refraction profiles this discontinuity is dipping towards northeast beneath the KBS station and is horizontal beneath the HSPB station. Based on RF study, d2 interface is dipping toward south-west beneath the HSPB station, and no clear evidence of its inclination is visible beneath the KBS station (Fig. 4). Previously, the Q- and T-RFs of HSPB station have been analyzed by Wilde-Piórko *et al.* (2009), but only one dipping discontinuity has been mapped because not enough data were available at that time.

The SPITS array is located in the Central Tertiary Basin (Hjeller 1983) and 1-D RF modelling suggested that in the upper and middle crust no contrasts of seismic velocities exist and S-wave velocities gradually increase with depth down to 16 km (black line in Fig. 8; Table 3). BARENTS50 model shows distinct boundaries at the depth of 7, 19 and 26 km (green line in Fig. 8). According to Klitzke *et al.* (2015) at this area the sediments (pre-mid-Permian megasequence) reach the depth of 8–10 km. At refraction profiles (Czuba 2013) for areas close to Billefjorden Fault Zone, two discontinuities are visible in the crust, first at the depth of 10 km and second at the depth of about 22 km. So, the surface wave analysis and deep seismic sounding profiling give consistent model of the structure at this area, which is not confirmed by RF calculation. The P-to-S converted phase from d1 discontinuity at the depth of 200 m beneath the SPITS array has amplitude of 0.04, while the P-to-S converted phases at the same discontinuity beneath the KBS and HSPB stations has amplitude of 0.06 and 0.07, respectively. It means the contrast of seismic velocities at shallow depth beneath the KBS and HSPB stations is larger than beneath the SPITS array. So, it could not be postulated that beneath the SPITS array strong contrast of seismic velocities at shallow depth produces the strong reverberation and mask the converted phases from deeper boundaries, because it is not observed for Q-RFs of the KBS and HSPB stations. The later amplitudes of Q-RFs of the SPITS array are about 0.02, while for other stations are 0.05 and 0.04.

Also, the back-azimuthal section of T-RF of the SPITS array shows high simplicity in comparison to the KBS and HSPB ones. Since the peak of phase d3 is twice as wide as the peaks of other phases, the seismic velocities grow monotonically with depth and a strong contrast of seismic velocities is not observed at the depth of 16 km beneath the SPITS array.

The crustal thickness estimated from Zhu and Kanamori method and 1-D forward modelling gave the same values and agreed very well with results of deep seismic sounding refraction measurements (Czuba *et al.* 2008; Czuba 2013; Krysiński *et al.* 2013). On the other hand, much larger deviation exists for regional models, *e.g.* the Moho depth based on the Moho depth map of the European Plate (Grad *et al.* 2009) are 30.2 ± 3.2 , 27.1 ± 3.2 km and 34.1 ± 4.0 km, respectively for the KBS and HSPB stations and the SPITS array, while from the RF modelling are 25 ± 3 , 32 ± 3 km and 33 ± 3 , respectively (Fig. 6, Table 3). For BARENTS50 model the Moho is shallower by about 8 and 4 km beneath the HSPB station and the SPITS array (Fig. 8 – green lines). Model of Klitzke *et al.* (2015) gives the thickness of the crust in 5 km interval, in good agreement with results of present study. The RFs of KBS station have been analysed before by Geissler *et al.* (2008), who also calculated the thickness of the crust to be 25 km.

Beneath the KBS station the image of structure is very complicated, because of the location of the seismic station next to Kongsfjorden/Forlandsundet Graben, where over 40 km along a refraction profile, P-wave seismic velocities lower by 0.5 km s^{-1} comparing to neighbouring areas are observed down to a depth of 20 km (Czuba 2013). Thus, seismic waves can impinge at large angle of incidence on a discontinuity separating medium with lower seismic velocities from medium with higher ones, giving the negative amplitude of Q-RF from the middle/lower crust (Figs 3 and 4). A stacked Q-RF of the KBS station (Fig. 3) used for 1-D forward modelling is greatly influenced by complicated 3D seismic structure beneath the station, so low velocities observed in lower crust beneath the KBS station from forward modelling of RF should be interpreted with caution. However, at the depths of 15–25 km, S-wave velocities of 3.5 km s^{-1} are observed also beneath the HSPB station (Fig. 8). The S-wave velocity of the BARENTS50 model (green line in Fig. 8) beneath the KBS and HSPB stations and the SPITS array are generally higher by about 0.5 km/s comparing to results of 1-D modelling of RF (green line in Fig. 8).

The uppermost mantle S-wave velocities obtained from 1-D modelling of RF are close to velocities obtained from the BARENTS50 model (green line in Fig. 8). However, beneath the SPITS array and HSPB stations, high and low S-wave velocities ($4.3\text{--}4.4 \text{ km s}^{-1}$ and $4.6\text{--}4.7 \text{ km s}^{-1}$) are observed down to depths of 100 and 75 km. Czuba (2013) reported the existence of uppermost mantle reflectors at the depth of about 40 km and 50 km in central part of north and south Spitsbergen what can be correlated with results of RF analysis. Surface waves analysis by Levshin *et al.* (2007) show lateral and vertical differentiation of S-wave velocities down to

the depth of 150 km in the south-central part of the Svalbard Archipelago. The S-wave velocities are decreasing from 4.6 km s^{-1} at the depth of 40 km to 4.4 km s^{-1} at the depth of 80–100 km and again increasing to 4.6 km s^{-1} at the depth of 150 km. At the same time, they are increasing from 4.4 km s^{-1} in the west to 4.6 km s^{-1} in the east of the Svalbard Archipelago at the depth of 80–100 km. Such complicated image of distribution of Vs can result in observed pattern of stacked Q-RF and influences the 1-D modelling of RF.

The spatial distribution of difference of observed delay time of P-to-S converted phases at “410 km” and “660 km” discontinuities and delay time calculated from the *iasp91* model is not uniform. For the “410 km” discontinuity almost no difference is observed, while for the “660 km” discontinuity, the area of Spitsbergen is divided into two parts: western and eastern (Fig. 9c and 9d). Geissler *et al.* (2008) reported that for the KBS station stacked P-to-S converted phase from the depth of 410 km comes a bit earlier comparing to the *iasp91* model. And for the depth of 660 km, he gives two numbers; in first case a converted phase comes a little bit earlier and in second case later comparing to the *iasp91* model. That observation can agree well with results of present study if the spatial distribution of delay time of phases is taken into account. The observed positive values (western part) can be related to lower S-wave velocities in the upper mantle and the crust comparing to the *iasp91* model or with larger depth of the mantle discontinuity; the negative values (eastern part) can be related to higher S-wave velocities in the upper mantle and the crust or with shallower depth of mantle discontinuity. The previous large-scale regional models (*e.g.* Pilidou *et al.* 2004; Kustowski *et al.* 2008) have shown no differences in S-wave velocity below the depth of 150 km. But the latest results of Legendre *et al.* (2012) have highlighted that the S-wave velocities from the depth of 150 km to the mantle transition zone are higher for the southern part of Archipelago than for central and northern parts. At the depths of 410 km and 585 km, the S-wave velocities are higher for the whole area of Svalbard with respect to reference model. These results correlate very well with observed delay times of P-to-S converted phases from the “410 km” discontinuity. On the other hand, they do not explain the observed delay times of converted phases from the “660 km”. That can indicate that mantle transition zone is thicker in western part of Svalbard and thinner in eastern part. It can be explained by character of the phase change of olivine – a hot mantle is associated with a thinner transition zone, and a cold mantle with a thicker transition zone (*e.g.* Bina and Helffrich 1994). However, it must be stated that the phases converted from the mantle transition zone beneath the Svalbard Archipelago are not clearly seen in slowness section plots (Fig. 5) and the observed stacked amplitudes of converted phases from the mantle discontinuities are very low (about 1/4 of amplitudes calculated from the *iasp91* model in Fig. 9a, b). That can suggest that the contrast of seismic velocities at considered discontinuities is much lower than in the *iasp91* model or what is much more likely – much stricter criterion for manual selection of Q-RFs is necessary to

observe clear P-to-S conversion phases from mantle discontinuities (*e.g.* Knapmeyer-Endun *et al.* 2013).

Conclusions

Receiver function analysis of seismograms of teleseismic P-wave recorded by the broad-band seismic stations located in the Svalbard Archipelago allowed to determine the structure of the crust and upper mantle in the area. The distribution of S-wave velocities in the crust differs very much for the West Spitsbergen Fold-and-Thrust Belt and the Central Tertiary Basin, *e.g.* near-surface S-wave velocities are $1,7 \pm 0,8$ and $1,0 \pm 0,5$ km s⁻¹, respectively. Back-azimuthal analysis of T-RFs allows for mapping of dipping discontinuities in the West Spitsbergen Fold-and-Thrust Belt. Estimated depth of Moho discontinuity is similar to results of refraction studies and quite different compared to regional models because of complex three-dimensional structure of this area. The crustal thickness determined by the Zhu and Kanamori method (2000) is 32 ± 3 km beneath the HSPB station (Poisson's ratio is $0,21 \pm 0,08$), 25 ± 3 km beneath the KBS station (Poisson's ratio is $0,28 \pm 0,07$) and 33 ± 3 km beneath the SPITS array (Poisson's ratio is $0,24 \pm 0,08$). The layering of uppermost mantle is observed for southern stations. The thickness of the mantle transition zone is larger for western part of archipelago and smaller for eastern part comparing to *iasp91* model.

Acknowledgements. — This research was financed from the NCN grant 2011/01/B/ST10/06653. The IRIS DMS is funded through the National Science Foundation and specifically the GEO Directorate through the Instrumentation and Facilities Program of the National Science Foundation under Cooperative Agreement EAR-0004370. I would like to thank Johannes Schweitzer for some data from the SPITS array. I would like also to thank Wolfram Geissler and an anonymous reviewer for their detailed and constructive comments which helped to improve this paper.

References

- AMMON C.J. 1991. The isolation of receiver effects from teleseismic P waveforms. *Bulletin of the Seismological Society of America* 81: 2504–2510.
- BERTEUSSEN K.A. 1977. Moho depth determinations based on spectral ratio analysis of NORSAR long-period P waves. *Physics of the Earth and Planetary Interiors* 31: 313–326.
- BINA C.R. and HELFFRICH G. 1994. Phase transition Clapeyron slopes and transition zone seismic discontinuity topography. *Journal of Geophysical Research* 99 (B8): 15853–15860.
- BIRKENMAJER K. 1981. The geology of Svalbard, the western part of Barents Sea and the continental margin of Scandinavia. In: A.E. Nairn, M. Churkin Jr. and F.G. Stehli (eds) *The Ocean Basins and Margins, The Arctic Ocean*, Plenum, New York; 5: 265–239.
- CASSIDY J.F. 1992. Numerical Experiment in Broadband Receiver Function Analysis. *Bulletin of the Seismological Society of America* 82: 1453–1474.

- CZUBA W. 2013. Seismic view on the Svalbard passive continental margin. *Acta Geophysica* 61 (5): 1088–1100.
- CZUBA W., GRAD M., GUTERCH A., MAJDAŃSKI M., MALINOWSKI M., MJELDE R., MOSKALIK M., ŚRODA P., WILDE-PIÓRKO M. and NISHIMURA Y. 2008. Seismic crustal structure along the deep transect Horsted'05, Svalbard. *Polish Polar Research* 29 (3): 279–290.
- GARDNER G.H.F., GARDNER L.W. and GREGORY A.R. 1974. Formation velocity and density – the diagnostic basics for stratigraphic traps. *Geophysics* 39: 770–780.
- GEISSLER W.H., KIND R. and YUAN X. 2008. Upper mantle and lithospheric heterogeneities in central and eastern Europe as observed by teleseismic receiver functions. *Geophysical Journal International* 174: 351–376.
- GEISSLER W.H., KÄMPF H., KIND R., BRÄUER K., KLINGE K., PLENEFISCH T., HORÁLEK J., ZEDNÍK J. and NEHYBKA V. 2005. Seismic location of a CO₂ source in the upper mantle of the western Eger rift, Central Europe. *Tectonics* 24 (5): 1–23.
- GRAD M., TIIRA T., BEHM M., BELINSKY A.A., BOOTH D.C., BRÜCKL E., CASSINIS R., CHADWICK R.A., CZUBA W., EGORKIN A.V., ENGLAND R.W., ERINCHEK Yu.M., FUGLER G.R., GACZYŃSKI E., GOSAR A., GRAD M., GUTERCH A., HEGEDÜS E., HRIBCOVÁ P., JANIK T., JOKAT W., KARAGIANNI E.E., KELLER G.R., KELLY A., KOMMINAHO K., KORJA T., KORSTRÖM J., KOSTYUCHENKO S.L., KOZLOVSKAYA E., LASKE G., LENKEY L., LUOSTO U., MAGUIRE P.K.H., MAJDAŃSKI M., MALINOWSKI M., MARONE F., MECHIE J., MILSHTEN E.D., MOTUZA G., NIKOLOVA S., OLSSON S., PASYANOS M., PETROV O.V., RAKITOV V.E., RAYKOVA R., RITZMANN O., ROBERTS R., SACHPAZI M., SANINA I.A., SXHMIDT-AURSCH M.C., SERRANO I., ŠPIČÁK A., ŚRODA P., ŠUMANOVAC F., TAYLOR B., TIIRA T., VEDRENTSEV A.G., VOZÁR J., WEBER Z., WILDE-PIÓRKO M., YEGOROVA T.P., YLINIEMI J., ZELT B. and ZOLOTOV E.E., 2009. The Moho depth map of the European Plate. *Geophysical Journal International* 176: 279–292.
- HARLAND W.B. 1997. The Geology of Svalbard. *Geological Society Memoir No. 17*. The Geological Society, London: 521 pp.
- HAUSER J., DYER K.M., PASYANOS M. E., BUNGUM H., FALEIDE J.I., CLARK S.A. and SCHWEITZER J. 2011. A probabilistic seismic model for the European Arctic. *Journal of Geophysical Research* 116: 1–17.
- HJELLE A. 1993. *The Geology of Svalbard*. Norsk Polarinstitut, Oslo: 163 pp.
- KENNETT B.L.N. and ENGDahl E.R. 1991. Traveltimes for global earthquakes location and phase identification. *Geophysical Journal International* 105: 429–465.
- KIND R., KOSAREV G.L. and PETERSEN N.V. 1995. Receiver functions at the stations of the German Regional Seismic Network (GRSN). *Geophysical Journal International* 121: 191–202.
- KLITZKE P., FALEIDE J.I., SCHECK-WENDEROTH M. and SIPPEL J. 2015. A lithosphere-scale structural model of the Barents Sea and Kara Sea region. *Solid Earth* 6: 153–172.
- KNAPMEYER-ENDRUN B., KRÜGER F., LEGENDRE C.P., GEISSLER W.H. and PASSEQ WORKING GROUP 2013. Tracing the influence of the Trans-European Suture Zone into the mantle transition zone. *Earth and Planetary Science Letters* 363: 73–87.
- KRYSIŃSKI L., GRAD M., MJELDE R., CZUBA W. and GUTERCH A. 2013. Seismic and density structure of the lithosphere-asthenosphere system along transect Knipovich Ridge-Spitsbergen-Barents Sea – geological and petrophysical implications. *Polish Polar Research* 34 (2): 111–138.
- KUSTOWSKI B., EKSTRÖM G. and DZIEWOŃSKI A. 2008. The shear-wave velocity structure in the upper mantle beneath Eurasia. *Geophysical Journal International* 17: 978–992.
- LANGSTON C.A. 1977. Corvallis, Oregon, crustal and upper mantle structure from teleseismic P and S waves. *Bulletin of the Seismological Society of America* 67: 713–724.
- LEGENDRE C.P., MEIER T., LEBEDEV S., FRIEDERICH W. and VIREECK-GÖTTE L. 2012. A shear-wave velocity model of the European upper mantle from automated inversion of seismic shear and surface waveforms. *Geophysical Journal International* 191: 282–304.

- LEVSHIN A.L., SCHWEITZER J., WEIDLE C., SHAPIRO N.M. and RITZWOLLER M.H. 2007. Surface wave tomography of the Barents Sea and surrounding regions. *Geophysical Journal International* 170: 441–459.
- MÜLLER G. 1985. The reflectivity method: a tutorial. *Journal of Geophysics* 58: 153–174.
- OWENS T.J., ZANDT G. and TAYLOR S.R. 1984. Seismic evidence for an ancient rift beneath the Cumberland Plateau, Tennessee: A detailed analysis of broadband teleseismic P waveforms. *Journal of Geophysical Research* 89: 7783–7795.
- PILIDOU S., PRIESTLEY K., GUDMUNDSSON O. and DEBAYLE E. 2004. Upper mantle S-wave speed heterogeneity and anisotropy beneath the North Atlantic from regional surface wave tomography: the Iceland and Azores plumes. *Geophysical Journal International* 159:1057–1076.
- RITZMAN O. and FALEIDE J.I. 2009. The crust and mantle lithosphere in the Barents Sea/Kara Sea region. *Tectonophysics* 470: 89–104.
- RITZMANN O., MAERCKLIN N., FALEIDE J., BUNGUM H., MOONEY W. and DETWEILER S. 2007. A three-dimensional geophysical model of the crust in the Barents Sea region: model construction and basement characterization. *Geophysical Journal International* 170: 417–435.
- SAUL J., KUMAR M.R. and SARKAR D. 2000. Lithospheric and upper mantle structure of the Indian Shield, from teleseismic receiver function. *Geophysical Research Letters* 27: 2357–2360.
- SELLEVOLL M.A., DUDA S.J., GUTERCH A., PAJCHEL J., PERCHUĆ E. and THYSSSEN F. 1991. Crustal structure in the Svalbard region from seismic measurements. *Tectonophysics* 189: 55–71.
- SOLHEIM A., FALEIDE J.I., ANDERSON E.S., VANNESTE K., ELVERHØI A., UENZELMANN-NEBEN G. and FORSBERG C.F. 1998. Late Cenozoic seismic stratigraphy and glacial geological development of the East Greenland and Svalbard-Barents Sea continental margins. *Quaternary Science Reviews* 17: 155–184.
- STAMMLER K. 1993. Seismic Handler – Programmable multichannel data handler for interactive and automatic processing of seismological analyses. *Computer and Geosciences* 2: 135–140.
- STEEL R., GJELBERG J., HELLAND-HANSEN W., KLEINSPEHN K., NØTTVEDT A. and RYE-LARSEN M. 1985. The Tertiary strike-slip basins and orogene belt of Spitsbergen. In: K. Biddle and N. Christie-Blick (eds) *Strike-slip Deformation, Basin Formation and Sedimentation. Society of Economic Paleontologists and Mineralogists Special Publication* 37: 339–359.
- TALWANI M. and ELDHOLM O. 1977. The evolution of the Norwegian-Greenland Sea: recent results and outstanding problems. *Geological Society of America Bulletin* 88: 969–999.
- VINNIK L.P. 1977. Detection of waves converted from P to SV in the mantle. *Physics of the Earth and Planetary Interiors* 15: 39–45.
- WESSELS P. and SMITH W.H.F. 1998. New, improved version of generic mapping tools released. *EOS, Transaction, American Geophysical Union* 79: 579.
- WILDE-PIÓRKO M., GRAD M., WIEJACZ P. and SCHWEITZER J. 2009. HSPB seismic broadband station in Southern Spitsbergen: First results on crustal and mantle structure from receiver functions and SKS splitting. *Polish Polar Research* 30 (4): 301–316.
- ZHU L. and KANAMORI H. 2000. Moho depth variation in southern California from teleseismic receiver functions. *Journal of Geophysical Research* 105: 2969–2980.

Received 20 November 2014

Accepted 26 May 2015